

NuSTAR monitoring of MAXI J1348-630: evidence of high density disc reflection

Sudip Chakraborty^{1*}, Ajay Ratheesh^{2,3}, Sudip Bhattacharyya¹, John A. Tomsick⁴,
Francesco Tombesi^{2,5,6,7}, Keigo Fukumura⁸, Gaurava K. Jaisawal⁹

¹*Department of Astronomy and Astrophysics, Tata Institute of Fundamental Research, 1 Homi Bhabha Road, Mumbai 400005, India*

²*Department of Physics, Tor Vergata University of Rome, via della Ricerca Scientifica 1, 00133, Rome, Italy.*

³*INAF-IAPS, Via del Fosso del Cavaliere 100, I-00133 Rome, Italy*

⁴*Space Sciences Laboratory, University of California Berkeley, 7 Gauss Way, Berkeley, CA 94720-7450, USA*

⁵*INAF - Astronomical Observatory of Rome, Via Frascati 33, I-00078 Monte Porzio Catone (Rome), Italy*

⁶*Department of Astronomy, University of Maryland, College Park, MD 20742, USA*

⁷*NASA/Goddard Space Flight Center, Greenbelt, MD 20771, USA*

⁸*James Madison University, 800 South Main Street, Harrisonburg, Virginia 22807, USA*

⁹*National Space Institute, Technical University of Denmark, Elektrovej 327-328, DK-2800 Lyngby, Denmark*

Accepted 2021 September 4. Received 2021 September 4; in original form 2021 April 25

ABSTRACT

We present the broadband spectral analysis of all the six hard, intermediate and soft state *NuSTAR* observations of the recently discovered transient black hole X-ray binary MAXI J1348-630 during its first outburst in 2019. We first model the data with a combination of a multi-colour disc and a relativistic blurred reflection, and, whenever needed, a distant reflection. We find that this simple model scheme is inadequate in explaining the spectra, resulting in a very high iron abundance. We, therefore, explore the possibility of reflection from a high-density disc. We use two different sets of models to describe the high-density disc reflection: RELXILL-based reflection models, and REFLIONX-based ones. The REFLIONX-based high-density disc reflection models bring down the iron abundance to around the solar value, while the density is found to be $10^{20.3-21.4}\text{cm}^{-3}$. We also find evidence of a high-velocity outflow in the form of ~ 7.3 keV absorption lines. The consistency between the best-fit parameters for different epochs and the statistical significance of the corresponding model indicates the existence of high-density disc reflection in MAXI J1348-630.

Key words: accretion, accretion discs — methods: data analysis — stars: black holes — X-rays: binaries — X-rays: individual: MAXI J1348-630

1 INTRODUCTION

Black hole X-ray binaries (BHBs) are systems with a black hole and a companion star. BHBs can be classified into persistent and transients based on the magnitude of flux change seen in them. In transient BHBs, the flux in the X-ray band can change by few orders of magnitude. The primary spectrum of BHBs can be modelled with a multi-temperature black body radiation emitted by an accretion disc (Novikov & Thorne 1973; Shakura & Sunyaev 1973), a Comptonisation (power-law) component due to the up-scattering of the soft disc photons in a high temperature compact structure called corona (Sunyaev & Titarchuk 1980, 1985), and a reflection of the Comptonized photons off the top layer of the disc. The reflection features consist of iron emission lines at 6 to 7 keV along with a

Compton hump at approximately 30-50 keV and an excess below 1 keV (Fabian 2016), further smeared by the relativistic effects in the vicinity of the black hole. The relativistic reflection component provides insights on the disc-corona geometry (such as the size of the coronal region and the inner radius of the disc) and the changes of inner accretion processes throughout the evolution of BHB spectral states. Thus the BHB spectral states are characterised by the geometry of the disc and corona, and the interplay between the direct and reflection components. The main spectral states of transient BHBs are the low hard state (LHS) and the high soft state (HSS) (Belloni et al. 2000). The main conjecture is that in the HSS the disc extends until inner most circular orbit (ISCO), while the disc is truncated at a larger distance in the LHS (Esin et al. 1997; Belloni et al. 2000; Ponti et al. 2012a). While transiting between these states, they undergo a q-shaped hysteresis within the hardness intensity diagram (HID) (Fender et al. 2004; Remillard & McClintock 2006). The

* E-mail: sudipchakraborty93@gmail.com

source rises in intensity from the LHS before transiting into the HSS, and then falls in intensity before transiting back into the low hard state before vanishing into quiescence. Outflows in the form of jet and winds are also observed in these systems. A jet is generally seen in the hard state and stronger while the source transits from soft to hard state (Fender et al. 2004). Even though disc winds are stronger in the soft state in comparison to the hard state (Ponti et al. 2012b; Fukumura et al. 2021; Ratheesh et al. 2021), the state dependence of disc wind is not clearly understood.

A common outcome of reflection modelling of BHB X-ray spectra is super-solar iron abundance (Parker et al. 2015; Walton et al. 2016). This high iron abundance is a feature seen in AGN as well (e.g., Parker et al. 2018). Radiative levitation, or the enhancement of the metallicity due to radiation-pressure dominance of the inner disc, has been proposed as an explanation behind these super-solar abundances (Reynolds et al. 2012). While in some AGN, this kind of high metallicity could indeed be real (Wang et al. 2012), in most of the cases, this is perhaps an artefact of the model and the assumptions therein. An alternate explanation of the high iron abundances involves reflection off a high-density accretion disc. For most of the widely used disc reflection models, a constant electron density of ($n_e = 10^{15} \text{cm}^{-3}$, inspired by the values observed in AGN) is assumed for the top layer of the disc, along with the assumption that the actual density does not have a significant effect on the predicted spectrum. While this density is appropriate for the very highest mass supermassive BHs in AGN (e.g., Grupe et al. 2010; Jiang et al. 2019b), BHBs may require higher densities (García et al. 2016). However, the free-free absorption and heating of the disc have both found to be quadratically dependent on density. As the density increases, the rise in free-free absorption leads to an increase in the temperature of the top layer of the disc, causing extra thermal emission and increasing the reflected emissions below 1 keV (Ross & Fabian 2007; García et al. 2016). Thus, models taking into account this effect has been demonstrated to relieve the very high iron abundance required in other reflection models (e.g., Tomsick et al. 2018; Jiang et al. 2019b).

MAXI J1348-630 is such a transient BHB discovered by Gas Slit Camera (GSC) onboard Monitor of All-sky X-ray Image (MAXI) (Matsuoka et al. 2009), and classified as a BHB based on the estimated mass and spectral features (Tominaga et al. 2020). Previous studies, using MAXI/GSC, *Swift*/XRT (Tominaga et al. 2020) and *NICER* data (Zhang et al. 2020), indicate that MAXI J1348-630 also exhibits a q-shaped hysteresis and that it is most likely a BHB. The source exhibited a hard to soft transition from MJD 58517 to MJD 58530 and returned back to the hard state around MJD 58600 (Tominaga et al. 2020). The distance to the source was estimated to be 3.39 kpc, based on the precise measurements using a dust scattering ring around the source (utilizing *SRG*/eROSITA and *XMM-Newton* data; Lamer et al. 2020). Monitoring of the inner disc radius from the spectral analysis indicate a black hole mass of $11 \pm 2 M_\odot$ (Tominaga et al. 2020; Lamer et al. 2020). Even during the soft state the inner disc temperature was in the range of 0.5 to 0.7 keV (Tominaga et al. 2020; Zhang et al. 2020). The source underwent a failed outburst without hard to soft transition as also seen previously in some transients BHBs (Tominaga et al. 2020; Homan et al. 2013; Fürst et al. 2015; Stiele & Kong 2020). The source showed type B quasi periodic oscillations (QPOs) during hard to soft transition generally accompanied by a relativistic jet (Belloni et al. 2020). The source was also detected in optical and ultraviolet (UV) and radio frequencies (Denisenko et al. 2019; Kennea & Negoro 2019;

Russell et al. 2019b,a).

In this present investigation, we provide a broadband spectral view of MAXI J1348-630, observed with the Nuclear Spectroscopic Telescope Array (*NuSTAR*, (Harrison et al. 2013b)) during its first complete outburst during January-June, 2019. With its pile-up free performance, reasonably good energy resolution (~ 400 eV at 10 keV) and sensitivity, *NuSTAR* provides an opportunity to study the relativistic reflection features along with a well-constrained inner disc radius and inclination with great precision. We use all the 6 *NuSTAR* data (see table 1) during the first outburst of MAXI J1348-630, spanning the hard, intermediate and soft states, and model the spectra with different disc reflection models. In particular, we focus on the possibility of high density reflection. The paper is organised as follows. In section 2.2, we describe the data reduction procedure of *NuSTAR*, as well as the MAXI/GSC and *Swift*/BAT lightcurves and HID of MAXI J1348-630. We then present an in-depth spectral analysis of *NuSTAR* data in section 3.1, first with regular density disc reflection models and then with high density reflection models in section 3.1.1 and 3.1.2. Finally, we summarise our results and discuss their implications in section 4.

2 OBSERVATIONS AND DATA REDUCTION

2.1 MAXI/GSC and *Swift*/BAT Lightcurve and HID

Since the BHBs evolve in timescales of the order of seconds to days, it is important to identify the state of the source based on continuous monitoring of the source. Daily monitoring of the X-ray sky have been possible due to the Neil Gehrels *Swift* Observatory (*Swift*/BAT: Krimm et al. 2013) in the hard X-ray band and Gas Slit Camera on board Monitor of All-sky X-ray Image in the soft X-ray band (MAXI/GSC: Matsuoka et al. 2009). The daily averaged lightcurves of *Swift*/BAT and MAXI/GSC have been obtained from <https://swift.gsfc.nasa.gov/results/transients/> and <http://maxi.riken.jp>. The top panel of Fig. 1 shows the *Swift*/BAT (grey) and MAXI/GSC (black) crab normalized lightcurves in 15-50 keV and 4-10 keV energy range, and the bottom panel shows the hardness ratio in 4-10 keV and 2-4 keV ranges. 1 Crab unit corresponds to $1.1 \times 10^{-8} \text{ergs s}^{-1} \text{cm}^{-2}$ and $9.2 \times 10^{-9} \text{ergs s}^{-1} \text{cm}^{-2}$ in the 4-10 keV and 2-4 keV energy bands covered by MAXI/GSC, and $1.3 \times 10^{-8} \text{ergs s}^{-1} \text{cm}^{-2}$ in the 15-50 keV energy band covered by *Swift*/BAT (Kirsch et al. 2005). The dotted lines indicate the start and stop of the hard to soft state transition obtained from Tominaga et al. (2020). The vertical coloured lines indicate the *NuSTAR* observations used in this analysis as outlined in the subsection below (also refer to table 1). Fig. 2, shows the hardness intensity diagram (HID). The soft and hard bands used for the hardness ratio is as same as the bottom panel of Fig. 1. The HID indicates that the source underwent a q-shaped hysteresis starting from the low hard state as generally seen in black hole X-ray binaries. The coloured points in the HID indicate the MAXI/GSC data on the days of the observations used in this work.

2.2 *NuSTAR*

MAXI J1348-630 was observed with *NuSTAR* (Harrison et al. 2013a) 6 times in 5 different epochs during its first complete outburst cycle in January-June, 2019. The details of the *NuSTAR* observations and their colour coding followed throughout the rest of

Instrument	Obs ID	Obs. date (yyyy-mm-dd)	Exposure (s)	Abbreviation	Epoch
<i>NuSTAR</i>	80402315002	2019-02-01	3038	Nu02 (maroon)	E1
<i>NuSTAR</i>	80402315004	2019-02-01	736	Nu04 (maroon)	E1
<i>NuSTAR</i>	80402315006	2019-02-06	4520	Nu06 (red)	E2
<i>NuSTAR</i>	80402315008	2019-02-11	4639	Nu08 (orange)	E3
<i>NuSTAR</i>	80402315010	2019-03-08	9714	Nu10 (cyan)	E4
<i>NuSTAR</i>	80402315012	2019-04-03	12490	Nu12 (darkblue)	E5

Table 1. *NuSTAR* observation details for MAXI J1348-630. We include only the observations considered in this work. The colours, mentioned within the brackets, indicate the corresponding observations in all the figures. The colours are in accordance with matplotlib colour palette.

this work, are presented in table 1. From figure 2, it can be seen that the epoch E1 (maroon data point; comprised of the two contemporaneous *NuSTAR* observations Nu02 and Nu04, as denoted in table 1) is located in the hard state, while the epoch E2 (red; comprised of the *NuSTAR* observation Nu06) is situated at the hard-soft transition in the HID. The epochs E3-E5 (orange, cyan and dark-blue points in figure 2) all belong to the soft state, with decreasing flux levels. The *NuSTAR* data are processed using v2.0.0 of the NuSTARDAS pipeline. We also use *NuSTAR* CALDB v20200813. A rip in the Multi Layer Insulation (MLI) at the exit aperture of the *NuSTAR* Optics Module A (OMA), aligned with detector focal plane module FPMA, occurred presumably in early 2017. This has resulted in increased photon fluxes through OMA, resulting in low energy (<10 keV, more prominent in softer energies) excesses in FPMA spectra, as compared to FMPB. This effect of reduction in MLI covering fraction has been taken care of by implementing (through the *numkarf* module in NuSTARDAS v2.0.0, as well as the latest CALDB) time/temperature dependent correction to the FPMA effective area using specific on-axis ARF files (Madsen et al. 2020). However, there exist pathological observations in which this correction falls short. For these individual cases, the *NuSTAR* SOC has provided an XSPEC multiplicative table model¹. We come across one such observation (Nu10/E4), and implement the suggested correction (see section 3.1). We filter background flares due to enhanced solar activity by setting `saacalc = 2`, `saamode = OPTIMIZED`, and `tentacle = no` in NUPIPELINE. Furthermore, due to the source being extremely bright, we used a modified value of the 'statusexpr' keyword in NUPIPELINE, `statusexpr="STATUS==b0000xxx00xxxx000"`, as suggested in the HEASARC *NuSTAR* analysis guide². The source spectra are extracted from circular regions of the radius 120'' centred on the source location. To avoid contamination by source photons from the extremely bright source regions, the background spectra are extracted from blank regions on the detector furthest from the source location. The spectra are grouped in *ISIS* (Houck & Denicola 2000) version 1.6.2-41 to have a signal-to-noise ratio of at least 25 per bin (15 in case of the fainter spectra in E5), to facilitate χ^2 fitting statistics.

3 DATA ANALYSIS AND RESULTS

The spectral fitting and statistical analysis are carried out using the XSPEC version v-12.11.0 (Arnaud 1996). For the joint fitting be-

¹ http://nustarsoc.caltech.edu/NuSTAR_Public/NuSTAROperationSite/mli.php
² <https://heasarc.gsfc.nasa.gov/docs/nustar/analysis/>

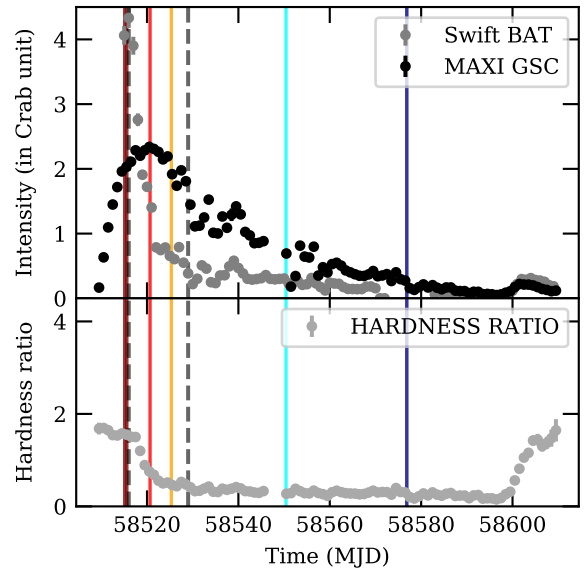


Figure 1. Top: *MAXI/GSC* (4-10 keV), *Swift/BAT* (15-50 keV) lightcurves are plotted in black and grey. Bottom: The corresponding hardness ratio (10-20 keV/4-10 keV) from *MAXI/GSC*. All the observations used in this analysis are marked by vertical colour shaded regions. The dotted lines indicate the start and stop of the hard to soft state transition.

tween FPMA and FMPB, a cross-normalisation constant (implemented using CONSTANT model in XSPEC) is allowed to vary freely for FMPB and is assumed to be unity for FPMA. To avoid the unexplained residuals below 4 keV in some of the observations, possibly related to the issue with the MLI blanketing as detailed in Madsen et al. (2020), an energy range between 4 keV and 79 keV is considered for the spectral fittings of all the epochs. To avoid the sharp instrumental features (as reported by Xu et al. (2018)), energies between 11-12 keV and 26-28 keV are excluded. All the models, as described below, include the Galactic absorption through the implementation of the TBABS model. The corresponding abundances are set in accordance with the Wilms et al. (2000) photoelectric cross-sections. The Galactic neutral hydrogen column density (N_H) is fixed to $8.6 \times 10^{21} \text{ cm}^{-2}$ (Tominaga et al. 2020) for all the described models. All parameter uncertainties are reported at the 90% confidence level for one parameter of interest. In addition to the χ^2 and the degrees of freedom, we also provide the null hypothesis probability for each of the models we use. In order to facilitate comparisons between the different nested and non-nested models and to select better models, we also state the Akaike Information Criterion (AIC, Akaike 1974) and Bayesian Information Criterion

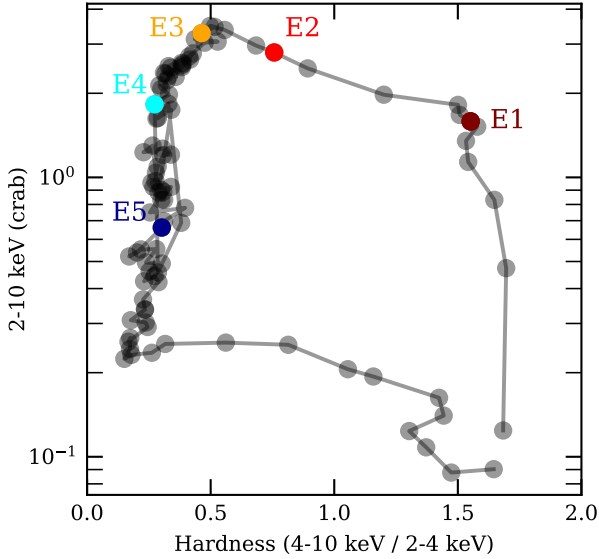


Figure 2. The hardness intensity diagram (HID) for MAXI J1348-630. For the hardness ratio 4-10 keV and 2-4 keV energy band in *MAXI/GSC* is taken as hard and soft bands respectively (in grey). The coloured points indicate the *MAXI/GSC* data during the *NuSTAR* observations used in this work.

(BIC, Schwarz 1978). AIC is more suitable to compare non-nested models, whereas BIC is more suited when nested models are compared (Kass & Raftery 1995), although that is not a necessity. In general, BIC penalises models with higher number of free parameters more severely. The AIC is defined as:

$$\text{AIC} = -2 \ln \mathcal{L} + 2k \quad (1)$$

where \mathcal{L} is the likelihood of the best-fit model, k is the number of free parameters. The BIC, on the other hand, is defined as:

$$\text{BIC} = -2 \ln \mathcal{L} + k \ln(N) \quad (2)$$

where N is the total number of data points. The values of the χ^2 for the best-fit models, χ^2_{\min} , in our fits can be converted to likelihood by equating the two: $\chi^2_{\min} = -2 \ln \mathcal{L}$. The values of AIC and BIC thus calculated for all our best-fit models, are provided in Tables 2, 3, 4 and 5. The model with the lowest AIC or BIC is the most preferred one. It should be noted, however, that the AIC and BIC compares models from pure statistical perspective; and one should also consider the physical interpretation of models and the reasonable range of their parameter values while selecting the ‘better’ model.

The spectra from all the epochs (E1 to E5) considered here are shown unfolded to a constant model in Figure 3 (left panel). A consistent spectral softening from hard to soft state can be observed. With our signal-to-noise ratio based binning, we find that the epochs E4 and E5 possess no statistically significant energy bins above 50 keV.

To highlight the spectral features more clearly, we plot the spectra from all the epochs as ratios to the best-fitting power-law model in Figure 3 (right panel). For the powerlaw fits, we only consider the energy intervals of 8-11 and 40-79 keV, where reflection from the disc has minimal effect. We then fit the 8-11,40-79 keV spectrum of each epoch with an absorbed cutoff power-law

model, `TBABSXCUTOFFPL` in XSPEC notation. Finally, we generate the 4-79 keV residuals by dividing the data from each epoch with the corresponding absorbed cutoff power-law model. The resulting figure 3 shows a broad Fe K- α emission line peaking around 6.5 keV and a Compton hump at \sim 20-40 keV for all the epochs, hinting the presence of relativistic reflection expected from an accretion disc extending close to a black hole (Fabian et al. 2000).

3.1 Quantitative modelling with reflection

For a detailed investigation of the broadband spectra including the reflection features, we start with the self-consistent relativistic disc reflection models from RELXILL model suite (relxill v1.3.10 : Dauser et al. (2014), García et al. (2014)). We assume an extended corona and use the model RELXILLCP which internally includes an thermal Comptonisation (NTHCOMP: Zdziarski et al. (1996), Życki et al. (1999)) continuum. Due to the strong degeneracy between the inner radius (R_{in}) of the accretion disc, and the dimensionless black hole spin parameter (a), we fit the data for R_{in} assuming a maximally spinning black hole ($a = 0.998$). We fix the outer edge of the accretion disc (R_{out}) at the maximum value for the model of $400R_g$ (where R_g is the gravitational radius of the black hole, defined as $R_g = GM/c^2$) and the emissivity indices at 3 ($q_1 = q_2 = 3$). On the other hand, we keep the inclination angle free. To account for the narrow core of the Fe-K α line in the hard state data (Epoch E1), we use the unblurred reflection model XILLVERCP (García & Kallman 2010). We use XILLVERCP only as a reflection component, freezing the refl_frac of XILLVERCP at -1, as only insignificant variations are found in the subsequent fits if the refl_frac is allowed to vary freely. We require an additional XILLVERCP for E3 as well. For both the cases, we assume the XILLVERCP component to be neutral to maintain simplicity. The electron temperatures (T_e), spectral indices (Γ), iron abundances (A_{Fe}) and inclinations (θ), are assumed to be equal between the RELXILLCP and XILLVERCP components. To model the soft X-ray excess (as evident from Figure 3), we use the multicoloured disc black-body (DISKBB: Mitsuda et al. (1984), Makishima et al. (1986)) model. As suggested by the instrument team, we also account for the MLI correction for FPMA in the pathological case of Nu10 (Epoch E4). This is done by the introduction of the multiplicative model NUMLIV1.MOD³ suggested by *NuSTAR* SOC (Madsen et al. 2020), and fixing the MLI covering fraction of FPMA to the recommended value of 0.83.

After the continua of all the epochs are modelled, absorption features around 7.2-7.3 keV are observed in the residuals for all of the 5 epochs. This kind of absorption features in the Fe-K band are commonly associated with blueshifted FeXXV/FeXXVI lines, and are believed to arise from absorption by outflowing material launched from the accretion disc (e.g., Ponti et al. 2012a). The narrow absorption line complex cannot be properly resolved by *NuSTAR*, hence we model it simply using a Gaussian absorption line model (GABS in XSPEC).

This constitutes our model M1 in Table 2:

Nu02/04/08:
TBabs×gabs×(diskbb+relxillCp+xillverCp)

Nu06/10/12:

³ http://nustarsoc.caltech.edu/NuSTAR_Public/NuSTAROperationSite/mliv1.php

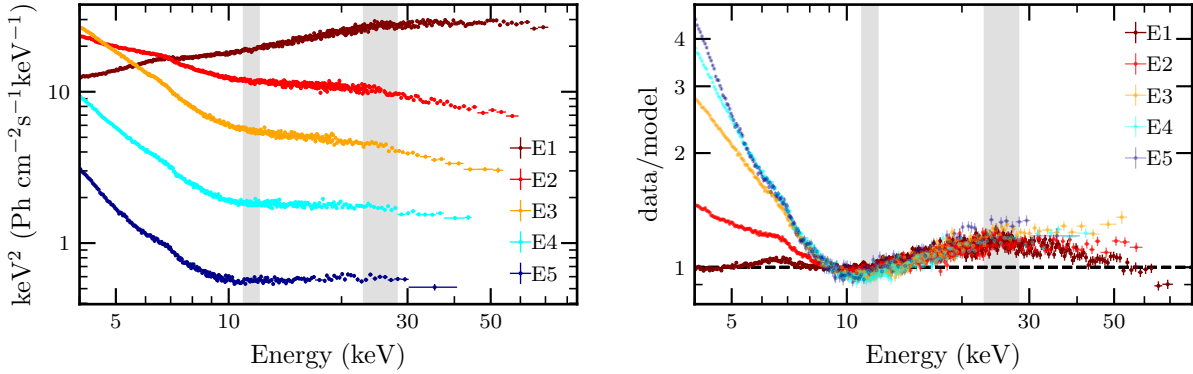


Figure 3. Left panel: *NuSTAR* spectra, unfolded with a `CONSTANT` model to see the spectral variations between the epochs. The colour coding for each epoch is detailed in table 1. Right panel: *NuSTAR* residuals, in form of data/model ratio, after a power-law fit. The soft excess, broad iron line and the Compton hump can be noticed. See section 3 for further details. The shaded grey region consists of energy bands ignored for detailed spectral fitting.

`TBabs×gabs×(diskbb+relxillCp)`

For epoch E1, the two *NuSTAR* observations (Nu02 and N04) are carried out within a short interval. For a consistent fit between the two observations, we allow the continuum parameters (Innermost temperature (T_{in}) of the `DISKBB` component, T_e and Γ of the `NTHCOMP` component in `RELXILLCP`) and all the normalisations to vary freely between them, tying up the absorption and reflection parameters (R_{in} , A_{Fe} , θ and ionisation parameter⁴ (ξ) of the `RELXILLCP` component) between the two observations.

From Table 2, we find that as the source moves from hard to soft states (E1 to E5), the T_{in} first increases before decreasing again, while the T_e increases before getting pegged at the parameter upper bound for `RELXILLCP` model. The disc is found to be highly ionised, and the inner edge of accretion disc is found to contract from $\sim 10R_g$ to near the innermost stable circular orbit (ISCO). The inclination is found to be around 30-45 degrees.

However, there are some problems with the best-fit M1 model, as apparent from Table 2. First of all, the iron abundance of the disc is found to be significantly higher than solar, sometimes pegging at the upper limit of 10 times solar. This fact is further verified by performing a Markov chain Monte Carlo (MCMC) analysis with 50 walkers with chain lengths of 5000 for E2, E4 and E5. These values are most likely overestimated, given the ubiquity of apparent super-solar iron abundances (García et al. 2018). The overestimate has previously been attributed to high density discs (Svensson & Zdziarski 1994; García et al. 2016) which would show stronger iron lines at a given metallicity (García et al. 2016; Tomsick et al. 2018). Secondly, this unusually high iron abundance is also found to be sometimes accompanied by systematically increasing residuals above 50 keV (see the uppermost panels showing the residuals in E3 and E4, in Figure 5). This feature has also been observed for Cyg X-1 by Tomsick et al. (2018). To address these issues, we subsequently explore the possibility of a high density disc by modeling all the *NuSTAR* spectra with high density reflection models.

⁴ Ionisation parameter is defined as $\xi = 4\pi F_X/n$, where F_X is the ionising continuum flux and n is the gas density

3.1.1 *relxill*-based high density reflection models

To extend the disc density from its constant value of $n_e = 10^{15} \text{cm}^{-3}$ to higher values, we first use the `RELXILL`-based high density reflection model, `RELXILLD`. In this model, the continuum is assumed to be a power-law with a high energy cutoff (`CUTOFFPL` in `XSPEC`), with the cutoff energy (E_{cut}) fixed at 300 keV. Instead, the disc density is treated as a free parameter, and can range from 10^{15}cm^{-3} to a maximum value of 10^{19}cm^{-3} . In case of E1 and E3, similar to M1, we add a neutral distant reflection as the best-fit model. To make the model consistent, we use the cutoff power-law version of the distant reflection component, `XILLVER`. All the parameters are treated in a similar manner as M1. Thus our model M2 (see Table 3) becomes: Nu02/04/08:

`TBabs×gabs×(diskbb+relxillD+xillver)`

Nu06/10/12:

`TBabs×gabs×(diskbb+relxillD)`

From Table 3 it can be seen that for the same degrees of freedom, best-fit M2 provides $\Delta\chi^2$ of 18-23 less than M1 for most of the epochs. For the hard state observations in E1, the fit gets worse due to kT_e being fixed at a high value of 300 keV. The iron abundances, except in E4, are brought down to more reasonable values of 1.5-4 times solar. All the continuum and reflection parameters follow a similar trend as M1, and the presence of the absorption line is also noted. The densities are consistently found to be much higher than the `RELXILLCP` value of 10^{15}cm^{-3} . Despite providing a better fit in general, we still face the problem of the disc densities pegging at the upper limit of 10^{19}cm^{-3} throughout E2 to E5.

3.1.2 *relflionx*-based high density reflection models

While `RELXILLD`-based model M2 provides a better fit than M1 and gives an indication of the presence of a high density disc, the disc density is found to peg at its upper limit of 10^{19}cm^{-3} . To circumvent this issue, we switch from the `RELXILL`-based `RELXILLD` to `RELFLIONX`-based (Ross & Fabian 2005) high-density reflection model `RELFLIONX_HD`, used by Tomsick et al. (2018) based on the code by Ross & Fabian (2007). `RELFLIONX_HD` assumes a cutoff power-law continuum and provides only the reflection component. As opposed to `RELXILLD`, `RELFLIONX_HD` has the disc density extending upto 10^{22}cm^{-3} . While similar to `RELXILLD`, `RELFLIONX_HD` has the cutoff

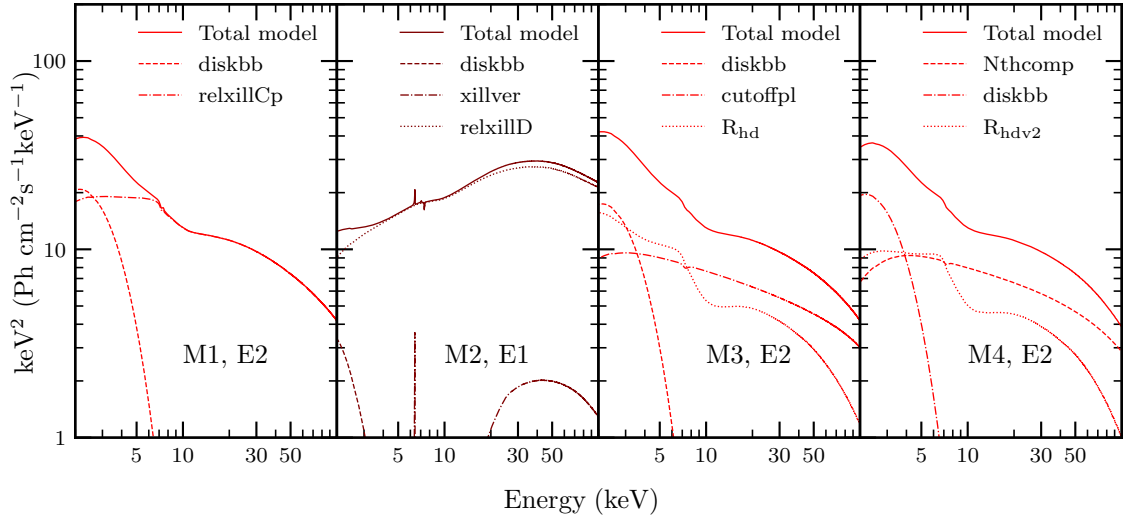


Figure 4. Best-fit models and model components for all the models (M1,M2,M3,M4), plotted for a representative epoch for each. The model corresponding model and epoch names are displayed in each panel. The bold, dashed, dotted and dash-dotted lines represent the total model, disc, relativistic blurred reflection and the unblurred distant reflection components, respectively. The epochs follow the colour coding from table 1. The spectral components are detailed in section 3.1, 3.1.1 and 3.1.2, and the implications discussed in section 4.

energy fixed at 300 keV, in case of `RELFIONX_HD` the iron abundance is also fixed at the solar value ($A_{\text{Fe}} = 1$). We convolve the `RELFIONX_HD` component with smeared relativistic accretion disc line profiles using `RELCONV` (Dauser et al. 2010). Thus, for E2-E5, `RELCONV*RELFIONX_HD` forms the reflection component, while we use `CUTOFFPL` as the direct component. Similar to M2, we also use an additional `XILLVER` component as required for epoch E3, the cutoff energy of which we also fix at 300 keV. For the hard state spectra in E1, with low cutoff energy of <32 keV, the assumption of $E_{\text{cut}} = 300$ keV might pose an issue. To take care of this issue, we introduce an exponential cutoff model `HIGECUT` to the reflection model, and use `NTHCOMP` as the continuum. Following the procedure adapted by Pintore et al. (2015), we fix the E_{cut} and E_{fold} energies in the `HIGECUT` model to the kT_e and $2.7 \times kT_e$ of the `NTHCOMP`, respectively. Additionally, we use `XILLVERCP` to account for the narrow core of the Fe-K emission. Thus, our model M3 (best-fit parameters detailed in Table 4) becomes:

Nu02/04:

`TBabs*gabs*(diskbb+Nthcomp+xillverCp+(higecut*relconv*reflionx_hd))`

Nu08:

`TBabs*gabs*(diskbb+cutoffpl+xillver+(relconv*reflionx_hd))`

Nu06/10/12:

`TBabs*gabs*(diskbb+cutoffpl+(relconv*reflionx_hd))`

It can be seen from Table 4 that M3 reduces the χ^2 values as compared to M2, by values between 1 and 46 for E2-E5, depending on the epoch, and by a value of 92 for E1. This improvement over M2 for one less free parameter for E2-E5 and 4 additional free parameters for E1, results in an improvement of the goodness of the fits. The trends in the continuum as similar to before, with the value of Γ for E1 being slightly harder than in M1 best-fit and kT_e attaining similar values. It is to be noted that the upper limit of the `CUTOFFPL` spectral index for `RELFIONX_HD` is 2.3. Thus, in case of E3

where the $\Gamma > 2.3$, we fix the Γ of the reflection component at 2.3 and allow the Γ of the direct `CUTOFFPL` component to vary freely. The disc density is found to be much higher than 10^{19}cm^{-3} , with values ranging in $0.7 - 27 \times 10^{20} \text{cm}^{-3}$. However, both the disc density and the ionization parameter are found to vary quite significantly between the observations. This could be an artefact of the modeling.

Although M3 provides a superior fit than M2, `RELFIONX_HD` still has a few limitations. Due to the cutoff energy being fixed at 300 keV, the hard state spectra cannot be consistently modeled with `RELFIONX_HD`. Furthermore, due to the upper limit of spectral index being fixed at 2.3, we are unable to constrain the value properly for E3. Finally, another crucial limitation of `RELFIONX_HD` is that the iron abundance is fixed at the solar value. Super-solar metallicity are quite common in X-ray binaries and are sometimes thought to be caused by radiative levitation (Reynolds et al. 2012).

For more flexible modelling, we use a more recent, `NTHCOMP` continuum-based high density reflection model `RELFIONX_HDV2` (John Tomsick, private communication). Here, the electron temperature and the iron abundance are free parameters, along with the other parameters present in `RELFIONX_HD`. Thus, our model M4 (see Table 5) becomes:

Nu02/04/08:

`TBabs*gabs*(diskbb+Nthcomp+xillverCp+(relconv*reflionx_hdv2))`

Nu06/10/12:

`TBabs*gabs*(diskbb+Nthcomp+(relconv*reflionx_hdv2))`

From Table 5, it can be seen that, statistically, M4 provides almost the same quality of fit as M3. The change in χ^2 is minimal, ranging from 1 to 10 for 2 degrees of freedom (1 degree of freedom in case of E1), even though the null hypothesis probability improves. In fact, the AIC and BIC actually increases for E4, while for E3 and E5 they are almost the same. However, as discussed in the beginning of section 3, we have to take into account the consistency of parameter values and their physical interpretation before selecting the optimal model. For M4, the values of kT_{in} and Γ are

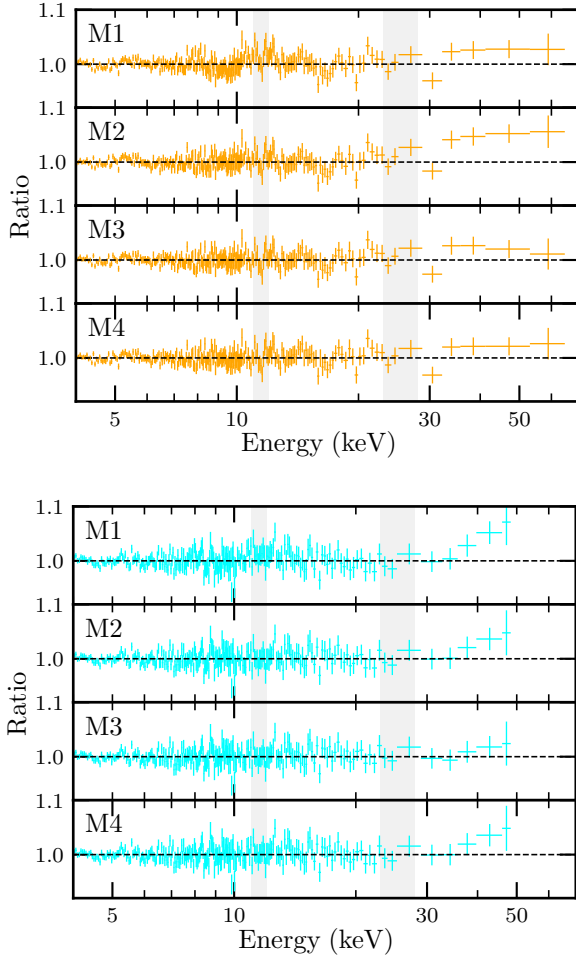


Figure 5. Residuals, in the form of data/model ratios, for each of the 4 models for two representative epochs E3 (orange, top panel) and E4 (cyan, bottom panel). For better visual representation, we display only the FPMA residuals. The light grey shaded regions indicate the 11.0-12.0 and 26.0-28.0 keV regions, ignored in this work due to unexplained systematics. See section 3.1 for model descriptions.

found to be broadly consistent between M4 and M3. Furthermore, the kT_e increases monotonically with time from $\sim 32 - 37$ keV to the maximum value of 400 keV from E1 to E5, while the R_{in} decreases from $\sim 13R_g \sim 2.6R_g$. Apart from E1 (for which the null hypothesis probability is still quite low), all the other inclinations are found to be consistent around 30-38 degrees. As in the case of M3, M4 also shows variations in ξ , although the variation is minimal between E2, E3 and E5. Furthermore, the iron abundances are also found to be consistent, hovering around the solar value. Apart from E4, the disc density are constrained to $\sim 10^{20.3-20.7} \text{ cm}^{-3}$ and are found to be consistent between all the epochs. The normalisations of the `REFLIONX_HDV2` components are found to monotonically decrease between E1 and E5. Finally, the absorption feature around 7.3 keV is found to be prominent and consistent across the epochs. For this consistency and the minimal statistical improvement, we can generally consider M4 as the most appropriate model. It can be observed, however, that for epoch E4, the density assumes a much higher value than the other observations or even compared to best-fit M3 model for E4. M4 also results in a slightly higher BIC and AIC for E4. Thus, even though M3 and M4 are almost equivalent

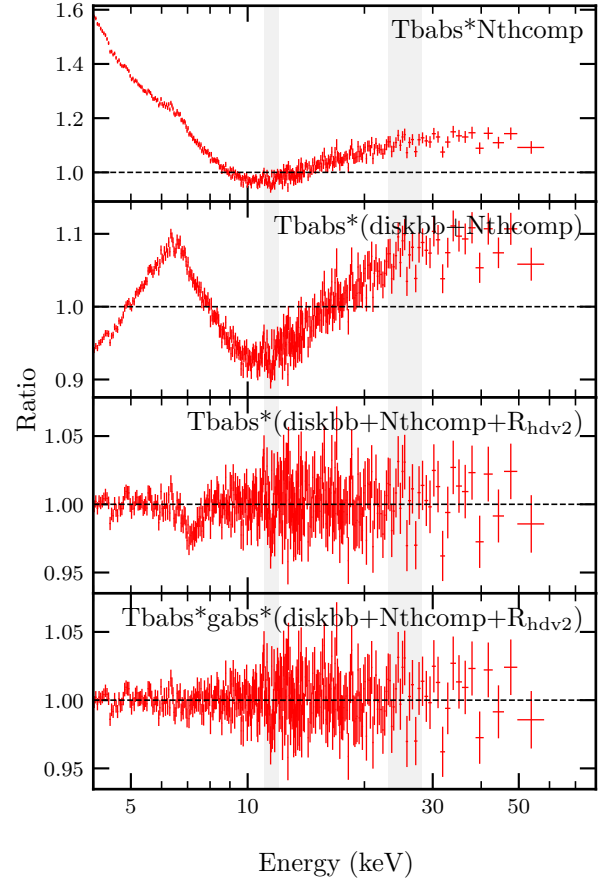


Figure 6. Residuals, in the form of data/model ratios, for different components of the best-fit model M4 for a representative epochs E2 (colour coded in accordance with table 1). For better visual representation, we display only the FPMA residuals. The panels, from top to bottom, demonstrate the improvement in residuals as further model components are added. R_{hdv2} abbreviates the reflection component, `RELCONV@REFLIONX_HD`. The light grey shaded regions indicate the 11.0-12.0 and 26.0-28.0 keV regions, ignored in this work due to unexplained systematics. See section 3.1 for model descriptions.

for E4, M3 can as well be considered a more consistent model for E4.

The models M1-M4, along with the individual components, are presented for a few representative epochs in Figure 4. The data/model ratios for all the models (M1-M4) are presented for the epochs E3 and E4 in Figure 5. The improvement in the fit residuals with the addition of different model components for the best-fit model M4, is presented for a representative epoch E2 in Figure 6.

4 DISCUSSIONS AND CONCLUSIONS

In this work, we present a consistent *NuSTAR* spectral analysis of the recently discovered BHB MAXI J1348-630, for 5 different epochs spanning hard, hard-soft transition and soft states during its first complete outburst in 2019. We model the *NuSTAR* spectra with the combination of a multi-coloured disc blackbody component, a Comptonisation continuum and `RELXILL`-based relativistic reflection components. The resulting model, M1 (see section 3.1 and table 2) proves quite inadequate to account for all the spec-

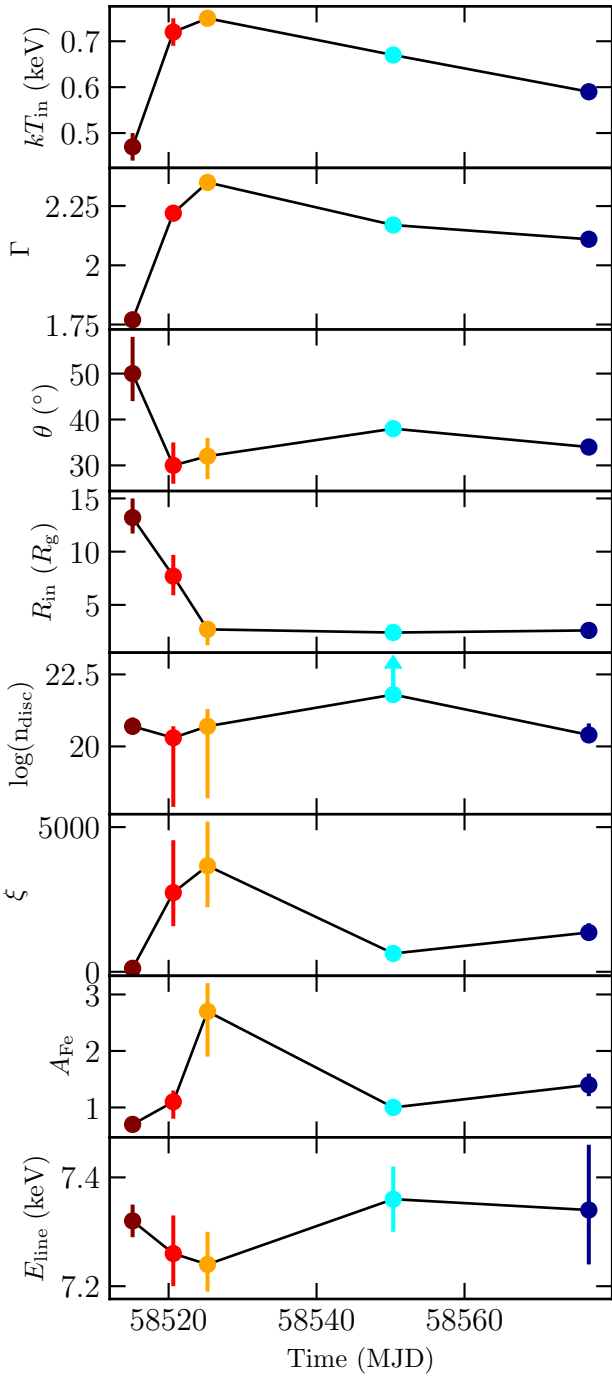


Figure 7. Time evolution of best-fit parameters for the best-fit model M4. The model is described in section 3.1.2, and the parameters are detailed in table 5. The data points are plotted for the different epochs following the colour scheme detailed in table 1.

tral features. Extremely high iron abundances, hints of high energy excess and low values of null hypothesis probabilities are found. There are a few scenarios that can explain the overabundance and the occasional high energy excesses. Presence of a jet, specially in the hard state, could explain some of the extreme parameters (Nowak et al. 2011). A jet has indeed been observed for MAXI J1348-630 by Carotenuto et al. (2021). However, jet models have

more free parameters, a comprehensive study of which is beyond our current work. One may try to approximate the presence of jet with the addition of an excess power-law or broken power-law component. However, this approach is found to lead to no further improvement for MAXI J1348-630. Alternately, presence of a second Comptonization region (Yamada et al. 2013; Basak et al. 2017; Chakraborty et al. 2020) has been proposed as the emission mechanism for MAXI J1348-630 (García et al. 2021). However, addition of a second corona component did not result in any significant improvement in our results. The third scenario, as investigated for other BHBs by Tomsick et al. (2018); Jiang et al. (2019a), could be high density reflection. In our current work, we explore this scenario in detail for MAXI J1348-630.

In section 3.1.1, we explore the high density ($n_e > 10^{15} \text{cm}^{-3}$) reflection in MAXI J1348-630 using the RELXILL-based RELXILLD model. The resulting model, M2 (best-fit parameters detailed in table 3), is found to yield statistically better fits. While M2 mostly resolves the issue with iron overabundance, the density is found to get pegged at the upper limit ($n_e = 10^{19} \text{cm}^{-3}$) of the model. Moreover, due to the electron temperature being fixed at 300 keV, RELXILLD is found to be inadequate for the hard state epoch E1. To better constrain the density, we then use the REFLIONX-based high density reflection models (see section 3.1.2). The resulting models, M3 and M4 (tables 4 and 5 details the best-fit parameter values), generate fits with AIC and BIC less than M1 or M2. The CUTOFFPL continuum-based REFLIONX_HD is limited by the facts that the iron abundance and the electron temperatures are fixed at the solar value and 300 keV, respectively. The latest, NTHCOMP continuum-based model REFLIONX_HDV2 alleviates these limitations. Although both M3 and M4 result in similar qualities of fits from a statistical point of view, M4 has more consistent parametrisation across the epochs. M3, however, results in a more consistent density value for the epoch E4, and a more consistent inclination for E1. The best-fit parameters for the most appropriate models (tables 4 and 5), are found to follow the following evolution (figure 7):

- The temperature of the innermost part of the accretion disc (kT_{in}) first increases to a maximum value of ~ 0.75 keV around the epoch E3, and then decreases. This trend exactly follows that found by Tominaga et al. (2020) and Zhang et al. (2020). The temporal evolution of Γ is also found to be similar to kT_{in} .
- The truncation radius of the inner accretion disc gets consistently closer to the black hole as the spectral state progresses from hard to soft state.
- The corona temperature increases from $\sim 32\text{--}37$ keV to a high value (pegged at the default maximal value of 400 keV for NTHCOMP) as the state goes from hard to soft.
- The inclination, apart from the hard state, is consistent between the observations. The low null hypothesis probability suggests that M4 may not be the most suitable model for hard state epoch E1. For all the other observations, the inclination is found to be $\sim 30\text{--}40$ degrees.
- The disc densities are more or less constant at $\sim 10^{(20.3\text{--}21.4)} \text{cm}^{-3}$. This kind of high disc density has previously been found in other BHBs (e.g., Tomsick et al. 2018; Jiang et al. 2019a).
- The abundances are found to be close to the solar value. This is in stark contrast with the RELXILL-based M1 model.

All these values are further supported by the MCMC analysis (appendix A). This consistency of the different parameters and steady improvement in reduced χ^2 for the high-density reflection models, gives further credence to our conclusion. García et al. (2016), however, emphasizes that the atomic physics underneath the the

reflection models is only known to be accurate up to densities of $\sim 10^{19}\text{cm}^{-3}$. Hence, more accurate determinations of the rates of atomic transitions and other quantities can have an impact on the high-density reflection models, thereby affecting our results.

As opposed to the RELXILLD, our RELCONV@REFLIONX_HD implementation is not fully self-consistent. In case of a real, extended accretion disc, the density should depend on the distance from the central compact object (Svensson & Zdziarski 1994). However, the REFLIONX_HD model assumes an optically thick, slab-like atmosphere of a constant density (Ross & Fabian 2005). Thus, in our implementation, the X-rays are assumed to be reflected from a single layer at a single photoionization radius (R_{ion} , Mori et al. (2019)). Therefore, following Mori et al. (2019), we perform a sanity check for the self-consistency of best-fit M4 model parameters. Assuming an isotropically emitting illuminating source (the corona), the ionisation parameter in REFLIONX_HD model can be re-defined as $\xi = \frac{L}{nR_{\text{ion}}^2}$ (where L is the illuminating luminosity, n is the hydrogen number density). Now, the electron density (n_e) quoted by REFLIONX_HD can be equated to the disc density (n_{disc}), as the accretion disc is believed to be primarily composed of hydrogen (this assumption has been followed throughout this work). Furthermore, we can use the 0.1-200 keV unabsorbed luminosity from the Comptonization and the reflection components (thus, disregarding the DISKBB) as a proxy for the illuminating luminosity L . This is found to be $\sim 1 \times 10^{37} - 3 \times 10^{38}$ ergs/s, depending on the epoch in consideration. Thus, using the values of n_{disc} and ξ from table 5, we can calculate R_{ion} as:

$$R_{\text{ion}} = \sqrt{\frac{L_{0.1-200\text{ keV}}^{\text{comp+refl}}}{n_{\text{disc}} \times \xi}} \quad (3)$$

On the other hand, we can utilize the inner radius of the accretion disc R_{in} as quoted by the RELCONV model from table 5. Therefore, assuming that the corona is located directly above the central black hole, $R_{\text{ion}} \gtrsim R_{\text{in}}$ can be imposed as a necessary self-consistency condition. Using the values from table 5, we find that for all our observations, this condition is satisfied within error bars.

The mass of MAXI J1348-630 has been reported to be $9.1^{+1.6}_{-1.2} M_{\odot}$ by Jana et al. (2020) and $13 \pm 2 M_{\odot}$ by Tominaga et al. (2020), further rectified to be $11 \pm 2 M_{\odot}$ by Lamer et al. (2020). Using equation 3 from Wang et al. (2018) and the correction factor from Kubota et al. (1998) for the soft state DISKBB normalisation, we find the black hole mass to be $\sim 11.6 - 19.4 M_{\odot}$. We note that the calculated mass from the *NuSTAR* DISKBB normalisation is likely to be incorrect, due to lack of <3 keV spectra in *NuSTAR*. Even though a simultaneous *Swift* -XRT or *NICER* data could be used to estimate the mass more accurately, we leave such a hard+soft X-ray spectral modelling for this source for a future work. For now, we use the black hole mass and distance estimates from Lamer et al. (2020). Using the Model M4, we find the integrated unabsorbed 0.1-200 keV luminosity of MAXI J1348-630 to be 1.3×10^{38} , 1.2×10^{38} , 1.4×10^{38} , 6.6×10^{37} and 3.3×10^{37} erg/s, for E1, E2, E3, E4 and E5, respectively. This implies that from E1 to E5, MAXI J1348-630 was accreting at 6 – 24% of the Eddington luminosity (L_{Edd}). Using the solution for radiation pressure-dominated disc from Svensson & Zdziarski (1994) (equation 1 in Garca et al. 2016), we can then explain the consistency of density between E1,E2 and E3, and the increase of density for E4. For a radiation-pressure dominated α -disc at high accretion rate (\dot{m} much larger than 0.1), $n_e \propto \dot{m}^{-2}$. Assuming an accretion efficiency ϵ to be 20% (Novikov & Thorne 1973; Agol & Krolik 2000), $\dot{m} = L_X/\epsilon L_{\text{Edd}} \approx L_{0.1-200\text{ keV}}/\epsilon L_{\text{Edd}}$. Using this relation, we

find an inverse relation between the X-ray luminosity L_X and the disc density. Therefore, for E1, E2 and E3 (where the 0.1-200 keV luminosity is found to be roughly the same), the disc density remains constant. The disc density then increases for E4, where the 0.1-200 keV luminosity decreases by a factor of 2. However, this does not explain the consistency between the densities derived for E5 and that of E1, E2 and E3.

Finally, another significant highlight of our work is the detection of absorption feature at ~ 7.3 keV throughout the epochs. Accounting for this feature, either using the multiplicative Gaussian absorption profile GABS or by using a Gaussian emission line profile with negative normalisation, improves the fit by $\Delta\chi^2 \sim 26-166$ (for 3 fewer degrees of freedom), indicating that the absorption feature is significantly detected. The lines are thus found to have equivalent widths (in absolute value) of $\sim 10-20$ eV. This kind of absorption lines are indication of outflows in the form of ionised accretion disc winds, believed to be ubiquitous in X-ray binaries (e.g., Ponti et al. 2012a) and important to the accretion process (Begelman et al. 1983). Disc winds in BHBs are generally known to have an equatorial geometry (e.g., Ponti et al. 2012a). However, recent evidences (Chiang et al. 2012; Xu et al. 2020; Wang et al. 2021) hint towards the existence of ultrafast winds even in non-equatorial directions. Among the prevalent driving mechanisms proposed, the thermally driven winds prefer high inclinations (Tomaru et al. 2020), while the MHD-driven winds can flow out at all directions (Fukumura et al. 2017). Therefore, the discovery of such a low-inclination ultrafast outflow as MAXI J1348-630, hints towards a magnetic origin (Chakraborty et al., in prep).

To summarise, we have characterised the broadband X-ray spectra of the recently-discovered transient black hole X-ray binary MAXI J1348-630 through systematic investigation of all the *NuSTAR* data during its first complete outburst in 2019. We find consistent continuum and reflection parameters, and the existence of an ultrafast outflow. We also find, using different RELXILL and REFLIONX-based reflection models, a significant evidence of reflection off a high density disc.

ACKNOWLEDGEMENTS

We thank the referee for constructive comments which improved the paper. This research has made use of the *MAXI* data provided by RIKEN, JAXA and the *MAXI* team. This research has also made use of the *NuSTAR* Data Analysis Software (NuSTARDAS), jointly developed by the ASI Science Data Center (ASDC, Italy) and the California Institute of Technology (USA). The authors also thank Samuzal Barua, Vikas Chand, and Mihoko Yukita for valuable insights and comments regarding data reduction and analysis. We thank Michael Parker for constructing the REFLIONX_HD and REFLIONX_HDV2 table models. JAT acknowledges partial support from NASA ADAP grant 80NSSC19K0586.

DATA AVAILABILITY

The observational data used in this paper are publicly available at NASA’s High Energy Astrophysics Science Archive Research Center (HEASARC; <https://heasarc.gsfc.nasa.gov/>). All the spectral figures are generated using the python implementation (pyxspect) of XSPEC. The MCMC results are plotted using the corner.py module (Foreman-Mackey 2016). Any additional information will be available upon reasonable request.

Table 2. Parameters of *NuSTAR* fits to MAXI J1348-630 spectra with model M1. The model M1 is detailed in section 3.1. Errors represent 90% confidence intervals.

Spectral Component	Parameter	Epoch				
		E1	E2	E3	E4	E5
diskbb	kT_{in} (keV)	$0.48^{+0.04}_{-0.07}$ (Nu02)	$0.69^{+0.02}_{-0.02}$	$0.80^{+0.01}_{-0.01}$	$0.69^{+0.01}_{-0.01}$	$0.59^{+0.01}_{-0.01}$
		$0.47^{+0.07}_{-0.08}$ (Nu04)
	norm ($\times 10^4$)	$1.1^{+1.0}_{-0.4}$ (Nu02)	$1.9^{+0.4}_{-0.3}$	$1.8^{+0.1}_{-0.1}$	$1.7^{+0.1}_{-0.1}$	$1.9^{+0.2}_{-0.1}$
		$1.2^{+0.5}_{-1.1}$ (Nu04)
relxillCp	Γ	$1.70^{+0.01}_{-0.01}$ (Nu02)	$2.22^{+0.01}_{-0.01}$	$2.36^{+0.01}_{-0.01}$	$2.18^{+0.01}_{-0.01}$	$2.09^{+0.05}_{-0.02}$
		$1.70^{+0.01}_{-0.01}$ (Nu04)
	kT_e (keV)	31^{+2}_{-3} (Nu02)	184^{+97}_{-34}	> 201	> 282	> 178
		28^{+2}_{-2} (Nu04)
	θ ($^\circ$)	42^{+4}_{-4}	37^{+2}_{-2}	42^{+1}_{-1}	35^{+2}_{-2}	31^{+2}_{-2}
	R_{in} (R_g)	$10.0^{+2.7}_{-4.0}$	< 2.7	$2.4^{+0.2}_{-0.2}$	$2.9^{+1.6}_{-1.3}$	< 3.2
	$\log \xi$ (log[erg cm/s])	$3.40^{+0.08}_{-0.10}$	$4.44^{+0.06}_{-0.07}$	$4.00^{+0.05}_{-0.08}$	$4.22^{+0.08}_{-0.06}$	$4.05^{+0.05}_{-0.15}$
	A_{Fe} ($A_{\text{Fe},\odot}$)	$1.4^{+0.5}_{-0.4}$	> 5.3	$4.1^{+0.4}_{-0.3}$	> 9.6	> 6.8
	\mathcal{R}	0.09	0.18	0.19	0.28	0.52
	norm	0.18 (Nu02)	0.19	0.13	0.03	0.06
		0.17 (Nu04)
xillverCp	norm ($\times 10^{-2}$)	1.0 (Nu02)	...	0.6
		0.7 (Nu04)
gabs	E_{line} (keV)	$7.26^{+0.07}_{-0.09}$	$7.21^{+0.04}_{-0.05}$	$7.16^{+0.04}_{-0.03}$	$7.26^{+0.18}_{-0.12}$	$7.19^{+0.11}_{-0.14}$
	σ_{line} (keV)	$0.14^{+0.08}_{-0.09}$	$0.11^{+0.05}_{-0.04}$	< 0.2	< 0.2	< 0.2
	line depth ($\times 10^{-2}$)	1.24	1.16	1.63	2.83	0.84
$\chi^2/\text{d.o.f.}$		2255/2029	1182/1036	884/804	784/722	721/714
null hypothesis probability		2.6×10^{-4}	1.0×10^{-3}	2.6×10^{-2}	5.3×10^{-2}	4.2×10^{-1}
AIC		2303.3	1209.9	917.6	812.5	749.0
BIC		2438.3	1279.3	997.6	876.9	813.2
Unabsorbed flux	C_{FPMB}	1.03	1.02	1.02	1.01	1.00
	3.0–70.0 keV ($\text{erg}/\text{cm}^2/\text{s}$)	1.13×10^{-7} (Nu02)	7.49×10^{-8}	5.59×10^{-8}	2.0×10^{-8}	6.6×10^{-9}
		1.13×10^{-7} (Nu04)

Note: T_{in} : Temperature of the inner disc; norm: Normalisation of the corresponding spectral parameter; Γ : Asymptotic power-law photon index; T_e : Electron temperature of the corona, determining the high energy rollover; θ : Inclination of the inner disc; R_{in} : Inner disc radius (in units of R_g); ξ : Ionisation parameter of the accretion disc, defined as $\xi = L/nR^2$, with L , n , R being the ionising luminosity, gas density and the distance to the ionised source, respectively; A_{Fe} : Iron abundance, in the units of solar abundance; \mathcal{R} : Reflection fraction; E_{line} : The central line energy for the Gaussian absorption model; σ_{line} : line width of the absorption line; C_{FPMB} : the flux normalisation constant for FPMB (determined by multiplicative ‘constant’ parameter in the spectral models), estimated with respect to the FPMA flux.

REFERENCES

- Agol E., Krolik J. H., 2000, *ApJ*, **528**, 161
 Akaike H., 1974, *IEEE Transactions on Automatic Control*, **19**, 716
 Arnaud K. A., 1996, in Jacoby G. H., Barnes J., eds, *Astronomical Society of the Pacific Conference Series Vol. 101, Astronomical Data Analysis Software and Systems V*. p. 17
 Basak R., Zdziarski A. A., Parker M., Islam N., 2017, *MNRAS*, **472**, 4220
 Begelman M. C., McKee C. F., Shields G. A., 1983, *ApJ*, **271**, 70
 Belloni T., Klein-Wolt M., Méndez M., van der Klis M., van Paradijs J., 2000, *A&A*, **355**, 271
 Belloni T. M., Zhang L., Kylafis N. D., Reig P., Altamirano D., 2020, *Monthly Notices of the Royal Astronomical Society*, **496**, 4366–4371
 Carotenuto F., et al., 2021, arXiv e-prints, p. arXiv:2103.12190
 Chakraborty S., Navale N., Ratheesh A., Bhattacharyya S., 2020, *MNRAS*, **498**, 5873
 Chiang C.-Y., Reis R. C., Walton D. J., Fabian A. C., 2012, *MNRAS*, **425**, 2436
 Dauser T., Wilms J., Reynolds C. S., Brenneman L. W., 2010, *MNRAS*, **409**, 1534

Table 3. Parameters of *NuSTAR* fits to MAXI J1348-630 spectra with model M2. The model M2 is detailed in section 3.1.1. Errors represent 90% confidence intervals.

Spectral Component	Parameter	Epoch				
		E1	E2	E3	E4	E5
diskbb	kT_{in} (keV)	$0.41^{+0.04}_{-0.04}$ (Nu02)	$0.65^{+0.02}_{-0.02}$	$0.75^{+0.01}_{-0.01}$	$0.68^{+0.01}_{-0.01}$	$0.60^{+0.01}_{-0.01}$
		$0.37^{+0.07}_{-0.06}$ (Nu04)
	norm ($\times 10^4$)	$4.2^{+4.9}_{-1.9}$ (Nu02)	$2.4^{+0.5}_{-0.4}$	$2.6^{+0.2}_{-0.2}$	$1.9^{+0.1}_{-0.1}$	$1.8^{+0.1}_{-0.1}$
		$10.6^{+9.7}_{-11.9}$ (Nu04)
relxillD	Γ	$1.55^{+0.01}_{-0.01}$ (Nu02)	$2.21^{+0.03}_{-0.01}$	$2.28^{+0.01}_{-0.01}$	$2.16^{+0.01}_{-0.01}$	$2.11^{+0.02}_{-0.02}$
		$1.55^{+0.01}_{-0.01}$ (Nu04)
	θ ($^\circ$)	23^{+3}_{-3}	36^{+2}_{-1}	24^{+2}_{-1}	26^{+2}_{-3}	31^{+1}_{-2}
	R_{in} (R_g)	$9.3^{+1.5}_{-1.2}$	< 4.2	$2.7^{+0.4}_{-0.3}$	$3.1^{+0.5}_{-0.5}$	< 3.4
	$\log \xi$ (log[erg cm/s])	$3.82^{+0.01}_{-0.02}$	$4.09^{+0.13}_{-0.06}$	$4.05^{+0.09}_{-0.10}$	$4.02^{+0.14}_{-0.09}$	$3.40^{+0.09}_{-0.17}$
	A_{Fe} ($A_{\text{Fe},\odot}$)	$1.6^{+0.1}_{-0.1}$	$4.0^{+0.9}_{-0.9}$	$3.4^{+0.4}_{-0.4}$	> 6.2	$3.8^{+1.5}_{-0.9}$
	$\log n_{\text{disc}}$ (log[cm^{-3}])	$17.8^{+0.2}_{-0.5}$	> 17.9	> 18.5	> 18.8	> 18.8
	\mathcal{R}	0.40	0.37	0.79	0.28	0.42
	norm	0.12 (Nu02)	0.16	0.06	0.03	0.01
		0.12 (Nu04)
	xillver	norm ($\times 10^{-2}$)	2.0 (Nu02)	...	0.5	...
1.8 (Nu04)		
gabs	E_{line} (keV)	$7.40^{+0.07}_{-0.41}$	$7.27^{+0.04}_{-0.05}$	$7.12^{+0.04}_{-0.05}$	$7.29^{+0.04}_{-0.04}$	$7.16^{+0.27}_{-0.05}$
	σ_{line} (keV)	< 0.2	$0.17^{+0.05}_{-0.06}$	< 0.2	$0.15^{+0.07}_{-0.05}$	< 0.2
	line depth ($\times 10^{-2}$)	0.93	1.53	1.3	1.80	0.63
$\chi^2/\text{d.o.f.}$		2348/2030	1164/1036	861/804	761/722	722/714
null hypothesis probability		1.1×10^{-5}	3.3×10^{-3}	7.9×10^{-2}	1.5×10^{-1}	4.1×10^{-1}
AIC		2356.4	1192.0	895.4	789.2	749.9
BIC		2485.9	1261.4	975.5	853.6	814.2
Unabsorbed flux	C_{FPMB}	1.03	1.02	1.02	1.00	1.00
	3.0–70.0 keV	1.13×10^{-7} (Nu02)	7.51×10^{-8}	5.64×10^{-8}	2.0×10^{-8}	6.65×10^{-9}
	($\text{erg}/\text{cm}^2/\text{s}$)	1.14×10^{-7} (Nu04)

Note: T_{in} : Temperature of the inner disc; norm: Normalisation of the corresponding spectral parameter; Γ : Asymptotic power-law photon index; θ : Inclination of the inner disc; R_{in} : Inner disc radius (in units of R_g); ξ : Ionisation parameter of the accretion disc, defined as $\xi = L/nR^2$, with L , n , R being the ionising luminosity, gas density and the distance to the ionised source, respectively; A_{Fe} : Iron abundance, in the units of solar abundance; n_{disc} : density of the top layer of the accretion disc, assumed to be equal to the corresponding electron number density; \mathcal{R} : Reflection fraction; E_{line} : The central line energy for the Gaussian absorption model; σ_{line} : line width of the absorption line; C_{FPMB} : the flux normalisation constant for FPMB (determined by multiplicative ‘constant’ parameter in the spectral models), estimated with respect to the FPMA flux.

Dauser T., Garcia J., Parker M. L., Fabian A. C., Wilms J., 2014, *MNRAS*, **444**, L100
 Denisenko D., et al., 2019, The Astronomer’s Telegram, **12430**, 1
 Esin A. A., McClintock J. E., Narayan R., 1997, *ApJ*, **489**, 865
 Fabian A. C., 2016, *Astronomische Nachrichten*, **337**, 375
 Fabian A. C., Iwasawa K., Reynolds C. S., Young A. J., 2000, *PASP*, **112**, 1145
 Fender R. P., Belloni T. M., Gallo E., 2004, *Monthly Notices of the Royal Astronomical Society*, **355**, 1105–1118
 Foreman-Mackey D., 2016, *The Journal of Open Source Software*, **1**, 24
 Fukumura K., Kazanas D., Shrader C., Behar E., Tombesi F., Contopoulos

I., 2017, *Nature Astronomy*, **1**, 0062
 Fukumura K., Kazanas D., Shrader C., Tombesi F., Kalapotharakos C., Behar E., 2021, arXiv e-prints, p. arXiv:2103.05891
 Fürst F., et al., 2015, *ApJ*, **808**, 122
 García J., Kallman T. R., 2010, *ApJ*, **718**, 695
 García J., et al., 2014, *ApJ*, **782**, 76
 García J. A., Fabian A. C., Kallman T. R., Dauser T., Parker M. L., McClintock J. E., Steiner J. F., Wilms J., 2016, *MNRAS*, **462**, 751
 García J. A., Kallman T. R., Bautista M., Mendoza C., Deprince J., Palmeri P., Quinet P., 2018, in Workshop on Astrophysical Opacities. p. 282 (arXiv:1805.00581)

Table 4. Parameters of *NuSTAR* fits to MAXI J1348-630 spectra with model M3. The model M3 is detailed in section 3.1.2. Errors represent 90% confidence intervals.

Spectral Component	Parameter	Epoch				
		E1	E2	E3	E4	E5
diskbb	kT_{in} (keV)	$0.47^{+0.09}_{-0.20}$ (Nu02)	$0.69^{+0.02}_{-0.02}$	$0.76^{+0.01}_{-0.01}$	$0.67^{+0.02}_{-0.02}$	$0.60^{+0.01}_{-0.02}$
		$0.43^{+0.09}_{-0.08}$ (Nu04)
	norm ($\times 10^4$)	$0.9^{+8.1}_{-0.2}$ (Nu02)	$1.5^{+0.9}_{-0.6}$	$2.1^{+0.1}_{-0.1}$	$2.0^{+0.4}_{-0.3}$	$1.8^{+0.4}_{-0.3}$
		$1.5^{+5.1}_{-0.7}$ (Nu04)
Nthcomp	Γ	$1.74^{+0.01}_{-0.01}$ (Nu02)
		$1.74^{+0.01}_{-0.01}$ (Nu04)
	kT_e (keV)	31^{+1}_{-1} (Nu02)
		29^{+1}_{-1} (Nu04)
cutoffpl	Γ	...	$2.23^{+0.02}_{-0.01}$	$2.40^{+0.02*}_{-0.02}$	$2.15^{+0.02}_{-0.03}$	$2.09^{+0.05}_{-0.05}$
relconv	θ ($^\circ$)	34^{+1}_{-1}	38^{+2}_{-3}	30^{+4}_{-12}	35^{+4}_{-4}	35^{+4}_{-4}
	R_{in} (R_g)	$8.6^{+1.6}_{-1.4}$	< 5.0	$3.0^{+0.4}_{-0.5}$	$2.5^{+0.1}_{-0.1}$	< 3.2
reflionx_hd	ξ (erg cm/s)	167^{+60}_{-51}	3652^{+545}_{-1002}	1608^{+663}_{-395}	796^{+398}_{-202}	1301^{+842}_{-816}
	n_{disc} ($\times 10^{20} \text{cm}^{-3}$)	$10.7^{+24.7}_{-7.7}$	$0.7^{+0.7}_{-0.3}$	$9.2^{+3.2}_{-2.7}$	$27.1^{+26.1}_{-14.5}$	$3.3^{+7.5}_{-1.9}$
	norm	60 (Nu02)	214	66	14	7.4
		55 (Nu04)
xillver(Cp)	norm ($\times 10^{-2}$)	0.2 (Nu02)	...	1.8
		0.2 (Nu04)
gabs	E_{line} (keV)	$7.00^{+0.04}_{-0.05}$	$7.36^{+0.05}_{-0.05}$	$7.27^{+0.07}_{-0.06}$	$7.39^{+0.05}_{-0.05}$	$7.38^{+0.15}_{-0.12}$
	σ_{line} (keV)	$0.27^{+0.04}_{-0.03}$	$0.26^{+0.06}_{-0.06}$	$0.13^{+0.09}_{-0.08}$	$0.25^{+0.08}_{-0.08}$	$0.26^{+0.14}_{-0.11}$
	line depth ($\times 10^{-2}$)	3.1	2.4	1.1	3.9	3.3
$\chi^2/\text{d.o.f.}$		2256/2026	1154/1037	815/805	756/723	720/715
null hypothesis probability		2.3×10^{-4}	6.4×10^{-3}	4.0×10^{-1}	1.9×10^{-1}	4.4×10^{-1}
AIC		2304.5	1179.8	846.9	781.9	746.0
BIC		2439.6	1244.2	922.2	841.7	805.7
Unabsorbed flux	C_{FPMB}	1.03	1.02	1.02	1.01	1.00
	3.0–70.0 keV ($\text{erg}/\text{cm}^2/\text{s}$)	1.13×10^{-7} (Nu02)	7.5×10^{-8}	5.6×10^{-8}	2.0×10^{-8}	6.7×10^{-9}
		1.13×10^{-7} (Nu04)

Note: T_{in} : Temperature of the inner disc; norm: Normalisation of the corresponding spectral parameter; Γ : Asymptotic power-law photon index; θ : Inclination of the inner disc; R_{in} : Inner disc radius (in units of R_g); ξ : Ionisation parameter of the accretion disc, defined as $\xi = L/nR^2$, with L , n , R being the ionising luminosity, gas density and the distance to the ionised source, respectively; n_{disc} : density of the top layer of the accretion disc, assumed to be equal to the corresponding electron number density; E_{line} : The central line energy for the Gaussian absorption model; σ_{line} : line width of the absorption line; C_{FPMB} : the flux normalisation constant for FPMB (determined by multiplicative ‘constant’ parameter in the spectral models), estimated with respect to the FPMA flux.

García F., Méndez M., Karpouzas K., Belloni T., Zhang L., Altamirano D., 2021, *MNRAS*, **501**, 3173
 Grupe D., Komossa S., Leighly K. M., Page K. L., 2010, *ApJS*, **187**, 64
 Harrison F. A., et al., 2013a, *ApJ*, **770**, 103
 Harrison F. A., et al., 2013b, *ApJ*, **770**, 103
 Homan J., Fridriksson J. K., Jonker P. G., Russell D. M., Gallo E., Kuulkers E., Rea N., Altamirano D., 2013, *ApJ*, **775**, 9
 Houck J. C., Denicola L. A., 2000, in Manset N., Veillet C., Crabtree D.,

eds, *Astronomical Society of the Pacific Conference Series Vol. 216, Astronomical Data Analysis Software and Systems IX*. p. 591
 Jana A., Debnath D., Chatterjee D., Chatterjee K., Chakrabarti S. K., Naik S., Bhowmick R., Kumari N., 2020, *ApJ*, **897**, 3
 Jiang J., Fabian A. C., Wang J., Walton D. J., García J. A., Parker M. L., Steiner J. F., Tomsick J. A., 2019a, *MNRAS*, **484**, 1972
 Jiang J., et al., 2019b, *MNRAS*, **489**, 3436
 Kass R. E., Raftery A. E., 1995, *Journal of the American Statistical Asso-*

Table 5. Parameters of *NuSTAR* fits to MAXI J1348-630 spectra with model M4. The model M4 is detailed in section 3.1.2. Errors represent 90% confidence intervals.

Spectral Component	Parameter	Epoch				
		E1	E2	E3	E4	E5
diskbb	kT_{in} (keV)	$0.47^{+0.03}_{-0.03}$ (Nu02)	$0.72^{+0.03}_{-0.03}$	$0.75^{+0.01}_{-0.01}$	$0.67^{+0.01}_{-0.01}$	$0.59^{+0.01}_{-0.01}$
		$0.46^{+0.03}_{-0.02}$ (Nu04)
	norm ($\times 10^4$)	$0.3^{+0.5}_{-0.2}$ (Nu02)	$1.4^{+0.2}_{-0.2}$	$2.5^{+0.2}_{-0.1}$	$2.0^{+0.2}_{-0.2}$	$2.0^{+0.2}_{-0.1}$
		$0.3^{+1.5}_{-0.2}$ (Nu04)
Nthcomp	Γ	$1.77^{+0.01}_{-0.01}$ (Nu02)	$2.22^{+0.03}_{-0.03}$	$2.35^{+0.03}_{-0.03}$	$2.17^{+0.01}_{-0.02}$	$2.11^{+0.02}_{-0.01}$
		$1.76^{+0.01}_{-0.01}$ (Nu04)
	kT_e (keV)	37^{+1}_{-1} (Nu02)	142^{+94}_{-26}	> 10	> 169	> 175
		32^{+2}_{-1} (Nu04)
relconv	θ ($^\circ$)	50^{+8}_{-6}	30^{+5}_{-4}	32^{+4}_{-5}	38^{+1}_{-1}	34^{+1}_{-1}
	R_{in} (R_g)	$13.2^{+1.8}_{-1.5}$	$7.7^{+2.0}_{-1.8}$	$2.7^{+0.5}_{-1.5}$	$2.4^{+0.6}_{-0.4}$	$2.6^{+0.3}_{-0.3}$
reflionx_hdv2	ξ (erg cm/s)	120^{+6}_{-6}	2736^{+1811}_{-1159}	3664^{+1527}_{-1435}	632^{+184}_{-208}	1358^{+320}_{-280}
	A_{Fe} ($A_{\text{Fe},\odot}$)	$0.7^{+0.1}_{-0.1}$	$1.1^{+0.2}_{-0.3}$	$2.7^{+0.5}_{-0.8}$	$1.0^{+0.1}_{-0.1}$	$1.4^{+0.2}_{-0.2}$
	$\log n_{\text{disc}}$ ($\log[\text{cm}^{-3}]$)	$20.7^{+0.3}_{-0.3}$	$20.3^{+0.4}_{-2.4}$	$20.7^{+0.6}_{-2.5}$	> 21.8	$20.4^{+0.4}_{-0.2}$
	norm	66 (Nu02)	27	15	3.6	3.1
		64 (Nu04)
xillverCp	norm ($\times 10^{-2}$)	1.3 (Nu02)	...	0.8
		0.7 (Nu04)
gabs	E_{line} (keV)	$7.32^{+0.03}_{-0.03}$	$7.26^{+0.07}_{-0.06}$	$7.24^{+0.06}_{-0.05}$	$7.36^{+0.06}_{-0.06}$	$7.34^{+0.12}_{-0.10}$
	σ_{line} (keV)	$0.26^{+0.04}_{-0.03}$	$0.22^{+0.07}_{-0.08}$	$0.13^{+0.07}_{-0.01}$	$0.23^{+0.06}_{-0.06}$	$0.22^{+0.13}_{-0.09}$
	line depth ($\times 10^{-2}$)	2.9	1.6	1.2	3.5	1.9
$\chi^2/\text{d.o.f.}$		2245/2025	1144/1035	810/803	757/721	719/713
null hypothesis probability		4.0×10^{-4}	1.0×10^{-2}	4.2×10^{-1}	1.7×10^{-1}	4.3×10^{-1}
AIC		2295.3	1173.6	846.3	786.9	748.6
BIC		2435.9	1248.0	931.0	855.9	817.4
Unabsorbed flux	C_{FPMB}	1.03	1.03	1.03	1.02	1.00
	3.0–70.0 keV	1.13×10^{-7} (Nu02)	7.5×10^{-8}	5.6×10^{-8}	2.0×10^{-8}	6.7×10^{-9}
	(erg/cm 2 /s)	1.13×10^{-7} (Nu04)

Note: T_{in} : Temperature of the inner disc; norm: Normalisation of the corresponding spectral parameter; Γ : Asymptotic power-law photon index; θ : Inclination of the inner disc; R_{in} : Inner disc radius (in units of R_g); ξ : Ionisation parameter of the accretion disc, defined as $\xi = L/nR^2$, with L , n , R being the ionising luminosity, gas density and the distance to the ionised source, respectively; A_{Fe} : Iron abundance, in the units of solar abundance; n_{disc} : density of the top layer of the accretion disc, assumed to be equal to the corresponding electron number density; E_{line} : The central line energy for the Gaussian absorption model; σ_{line} : line width of the absorption line; C_{FPMB} : the flux normalisation constant for FPMB (determined by multiplicative ‘constant’ parameter in the spectral models), estimated with respect to the FPMA flux.

ciation, 90, 773
 Kennea J. A., Negoro H., 2019, The Astronomer’s Telegram, 12434, 1
 Kirsch M. G., et al., 2005, in Siegmund O. H. W., ed., Society of Photo-Optical Instrumentation Engineers (SPIE) Conference Series Vol. 5898, UV, X-Ray, and Gamma-Ray Space Instrumentation for Astronomy XIV. pp 22–33 (arXiv:astro-ph/0508235), doi:10.1117/12.616893
 Krimm H. A., et al., 2013, ApJS, 209, 14
 Kubota A., Tanaka Y., Makishima K., Ueda Y., Dotani T., Inoue H., Ya-

maoka K., 1998, PASJ, 50, 667
 Lamer G., Schwobe A. D., Predehl P., Traulsen I., Wilms J., Freyberg M., 2020, arXiv e-prints, p. arXiv:2012.11754
 Madsen K. K., Grefenstette B. W., Pike S., Miyasaka H., Brightman M., Forster K., Harrison F. A., 2020, arXiv e-prints, p. arXiv:2005.00569
 Makishima K., Maejima Y., Mitsuda K., Bradt H. V., Remillard R. A., Tuohy I. R., Hoshi R., Nakagawa M., 1986, ApJ, 308, 635
 Matsuoka M., et al., 2009, PASJ, 61, 999

- Mitsuda K., et al., 1984, *PASJ*, **36**, 741
Mori K., et al., 2019, *ApJ*, **885**, 142
Novikov I. D., Thorne K. S., 1973, in *Black Holes (Les Astres Occlus)*. pp 343–450
Nowak M. A., et al., 2011, *ApJ*, **728**, 13
Parker M. L., et al., 2015, *ApJ*, **808**, 9
Parker M. L., Miller J. M., Fabian A. C., 2018, *MNRAS*, **474**, 1538
Pintore F., et al., 2015, *MNRAS*, **450**, 2016
Ponti G., Fender R. P., Begelman M. C., Dunn R. J. H., Neilsen J., Coriat M., 2012a, *MNRAS*, **422**, L11
Ponti G., Fender R. P., Begelman M. C., Dunn R. J. H., Neilsen J., Coriat M., 2012b, *MNRAS*, **422**, L11
Rathesh A., Tombesi F., Fukumura K., Soffitta P., Costa E., Kazanas D., 2021, *A&A*, **646**, A154
Remillard R. A., McClintock J. E., 2006, *ARA&A*, **44**, 49
Reynolds C. S., Brenneman L. W., Lohfink A. M., Trippe M. L., Miller J. M., Fabian A. C., Nowak M. A., 2012, *ApJ*, **755**, 88
Ross R. R., Fabian A. C., 2005, *MNRAS*, **358**, 211
Ross R. R., Fabian A. C., 2007, *MNRAS*, **381**, 1697
Russell T., Anderson G., Miller-Jones J., Degenaar N., Eijnden J. v. d., Sivakoff G. R., Tetarenko A., 2019a, *The Astronomer’s Telegram*, **12456**, 1
Russell D. M., Al Yazeedi A., Bramich D. M., Baglio M. C., Lewis F., 2019b, *The Astronomer’s Telegram*, **12829**, 1
Schwarz G., 1978, *Annals of Statistics*, **6**, 461
Shakura N. I., Sunyaev R. A., 1973, *A&A*, **500**, 33
Stiele H., Kong A. K. H., 2020, *ApJ*, **889**, 142
Sunyaev R. A., Titarchuk L. G., 1980, *A&A*, **500**, 167
Sunyaev R. A., Titarchuk L. G., 1985, *A&A*, **143**, 374
Svensson R., Zdziarski A. A., 1994, *ApJ*, **436**, 599
Tomaru R., Done C., Ohsuga K., Odaka H., Takahashi T., 2020, *MNRAS*, **494**, 3413
Tominaga M., et al., 2020, *ApJ*, **899**, L20
Tomsick J. A., et al., 2018, *ApJ*, **855**, 3
Walton D. J., et al., 2016, *ApJ*, **826**, 87
Wang H., Zhou H., Yuan W., Wang T., 2012, *ApJ*, **751**, L23
Wang Y., Méndez M., Altamirano D., Court J., Beri A., Cheng Z., 2018, *MNRAS*, **478**, 4837
Wang Y., et al., 2021, *ApJ*, **906**, 11
Wilms J., Allen A., McCray R., 2000, *ApJ*, **542**, 914
Xu Y., et al., 2018, *ApJ*, **852**, L34
Xu Y., Harrison F. A., Tomsick J. A., Walton D. J., Barret D., García J. A., Hare J., Parker M. L., 2020, *ApJ*, **893**, 30
Yamada S., Makishima K., Done C., Torii S., Noda H., Sakurai S., 2013, *PASJ*, **65**, 80
Zdziarski A. A., Johnson W. N., Magdziarz P., 1996, *MNRAS*, **283**, 193
Zhang L., et al., 2020, *MNRAS*, **499**, 851
Życki P. T., Done C., Smith D. A., 1999, *MNRAS*, **309**, 561

APPENDIX A: MCMC RESULTS

To estimate better errorbars for some of the most important quantities for our model M4, we perform a Markov chain Monte Carlo (MCMC) analysis by using the XSPEC implementation of the EMCEE code (`xspec_emcee`⁵), written by Jeremy Sanders. We use the Goodman–Weare algorithm, with 50 walkers, chain lengths of 5000, and burn-in lengths of 500. The results of the MCMC are plotted in figures A1, A2, A3, A4 and A5. The contours denote the 1, 2 and 3- σ confidence contours for the 2D posterior distributions, while the value and errors quoted are the mean and 68% confidence levels for the 1D posterior distributions. The values are consistent with our spectral fits and gives further credence to our results.

⁵ https://github.com/jeremysanders/xspec_emcee

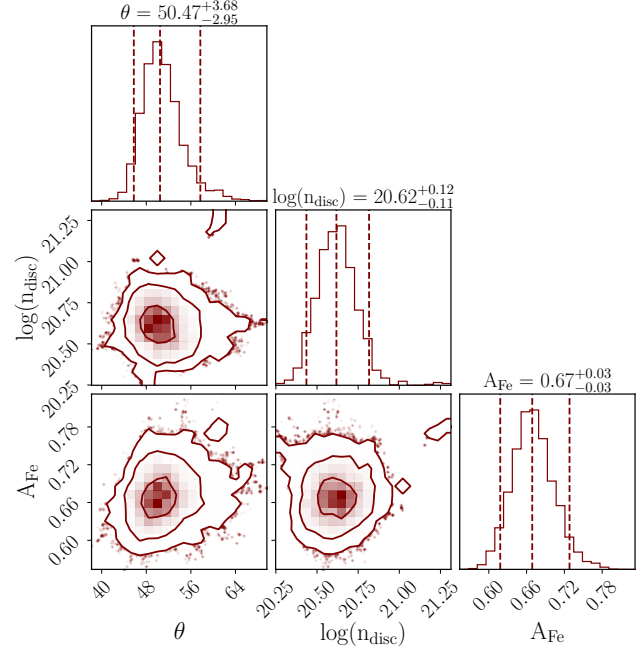


Figure A1. MCMC results for the epoch E1 and best-fit model M4.

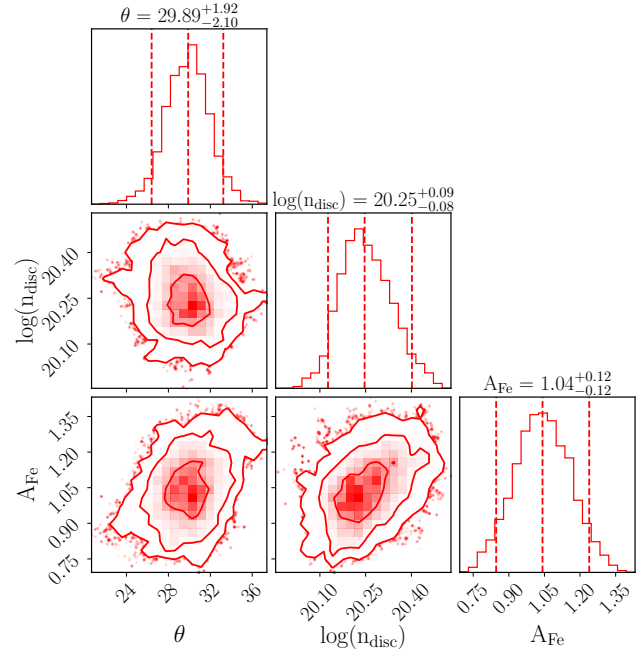


Figure A2. MCMC results for the epoch E2 and best-fit model M4.

This paper has been typeset from a \LaTeX file prepared by the author.

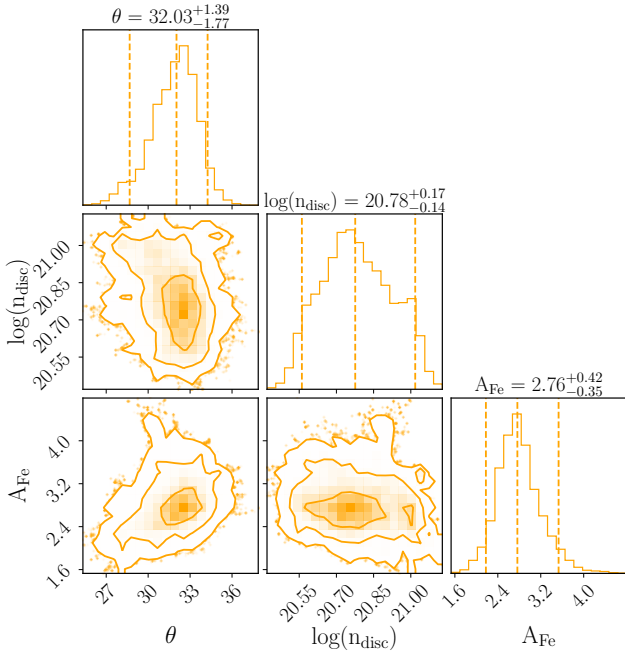


Figure A3. MCMC results for the epoch E3 and best-fit model M4.

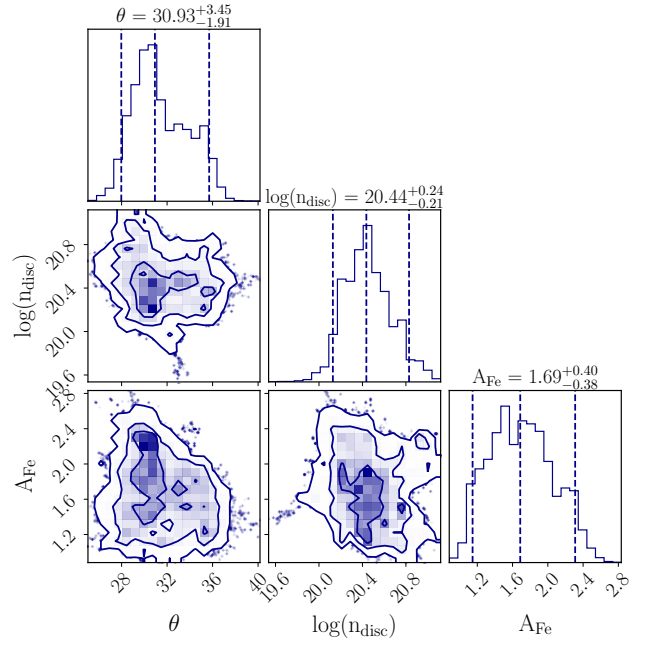


Figure A5. MCMC results for the epoch E5 and best-fit model M4.

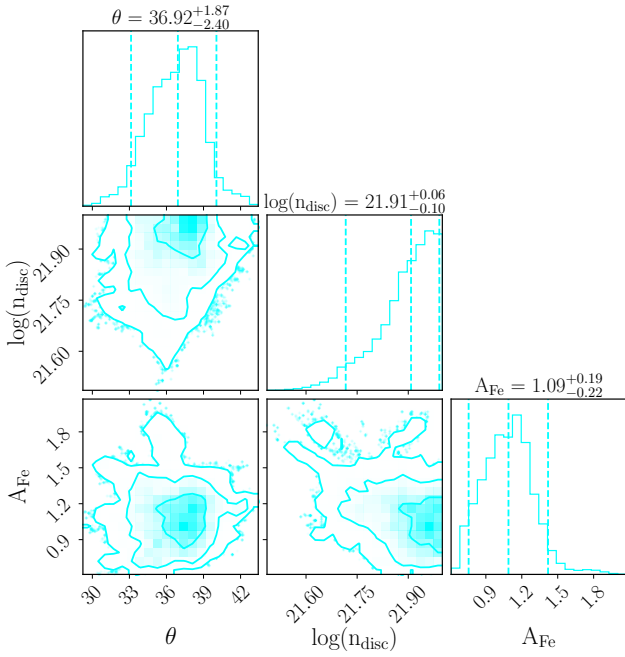


Figure A4. MCMC results for the epoch E4 and best-fit model M4.